Disturbed flow disrupts the blood-brain barrier in a 3D bifurcation model

Nesrine Bouhrira[1], Brandon J. DeOre[1], Daniel W. Sazer[2], Zakary Chiaradia[1], Jordan S. Miller[2], Peter A. Galie[1]

1. Department of Biomedical Engineering, Rowan University, Glassboro, NJ 08028
2. Department of Bioengineering, Rice University, Houston, TX 77005

Corresponding author:
Peter Galie, PhD
galie@rowan.edu
Dept. of Biomedical Engineering
Rowan University

Abstract

The effect of disturbed flow profiles on the endothelium have been studied extensively in systemic vasculature, but less is known about the response of the blood-brain barrier (BBB) to these flow regimes. Here we investigate the effect of disturbed flow on the integrity of the BBB using a three-dimensional, perfusable bifurcation model consisting of a co-culture of endothelial cells with mural and glial cells. Experimental flow patterns predicted by computational fluid dynamics mimic in vivo flow regimes, specifically the presence of a recirculation zone immediately downstream of the bifurcation. Dextran permeability assays and immunostaining with markers for tight junctions show that barrier disruption is significantly greater in areas of disturbed flow compared to fully developed regions downstream of the bifurcation. Probing crosstalk between cell types suggests that disturbed flow causes barrier breakdown independent of endothelial-mural and endothelial-glial interaction. Overall, disturbed flow-induced disruption of the blood-brain barrier suggests that flow-mediated mechanisms may contribute to vascular pathologies in the central nervous system.

Keywords: Blood-Brain Barrier, Vascular Model, Fluid Dynamics
Short Title: Disturbed flow disrupts the blood-brain barrier

Introduction

The pathological response of the endothelium to disturbed flow has been well documented, but less is known about its effects in the brain where endothelial cells feature tight junctions that give rise to the blood-brain barrier (BBB) (1-3). As shown in previous studies, disturbed flow forms primarily at the areas of arterial bifurcations due to the higher Reynolds number of the blood flow and a tendency to separate from the wall at these locations (4, 5). The shear stress exerted by disturbed flow is reduced in magnitude and oscillatory due to the presence of recirculation eddies that form downstream of the separated flow (6, 7). Previous investigations of systemic vasculature have found evidence that altered shear stress contributes to vascular dysfunction (8, 9): endothelial cells in both the separation zone and reattachment point exhibit modified gene expression (10-15). Furthermore, studies demonstrate that the shear stress profile adjacent to bifurcations destabilizes cell-cell and cell-matrix adhesions (16). In the brain, disruption of the cell-cell junctions causes breakdown of the BBB, exacerbating the pathological effects of disturbed flow. Yet the effect of altered shear stress on BBB integrity has not been interrogated directly.

There is growing evidence suggesting that the integrity of the BBB is sensitive to the mechanical stress applied by blood flow. Changes in blood flow have been associated with BBB disruption in several pathologies including dementia and Alzheimer's (17), epilepsy (18, 19) and in the aftermath of ischemia/reperfusion injury (20). Moreover, in vitro studies have shown that formation and maintenance of the blood-brain barrier in microvascular models requires exposure to fluid shear stress (21, 22). However, the integrity of the barrier is crucial not only in the microvasculature within the brain parenchyma, but also the larger pial and cerebral arteries in the subarachnoid space (23). In these vessels, the BBB is exposed to higher Reynolds numbers and therefore there is potential for disturbed flow, especially at arterial bifurcations. Evidence that the incidences of aneurysms and endothelial dysfunction are higher at bifurcations in cerebral arteries (24, 25) suggests that altered shear stress may disrupt the BBB at these locations. Therefore, interrogating the response of the BBB to these flow regimes may yield insight into the pathogenesis of vascular-related diseases in the brain.

Due to the complexity of the in vivo environment, in vitro models provide helpful tools to investigate the effects of disturbed flow on the BBB. However, the Reynolds number of fluid flows that separate from the wall exceeds the flow regimes that are achievable in previously published vascular models (26, 27). Recent advances in vascular patterning have enabled the development of in vitro models that can closely mimic in vivo geometries and microenvironments and facilitate high Reynolds number flow regimes (28). These advances can build upon previous BBB models that have relied on two-dimensional geometries (29, 30) or used three-dimensional models that mimic small diameter vessels by co-culturing endothelial cells with astrocytes or pericytes (22, 31-34). Here, both glial and mural cells are incorporated into a co-culture model with the endothelium to approximate the vessel architecture that experiences disturbed flow in vivo, since larger arteries exhibit a prominent mural layer that supports the augmented pressure differences incurred by higher flow rates. An annulus of smooth muscle cells surrounds the endothelial lumen, and the annulus itself is surrounded by an astrocyte-seeded hydrogel, to approximate the arrangement of these cells in vivo (35, 36). Furthermore, the vessels are patterned within a microfluidic device that is capable of applying fluid flow with a sufficiently high Reynolds number to separate from the wall of the endothelial lumen, yielding an experimental setup that can directly interrogate the response of the BBB to altered shear stress.

Materials and Methods

i. Microfabrication of microfluidic devices

Polydimethylsiloxane (PDMS) microfluidic devices were manufactured by soft lithography using a previously described protocol (22). Briefly, SU-8 2025 photoresist (MicroChem) was deposited on a silicon wafer and exposed to a UV source through a mask with the desired geometry. The inlet was positioned at an angle of 45 degrees to induce separated flow within the range of Reynolds numbers appropriate for modeling arterial blood flow (Re = 50-200). PDMS was used to cast negative and positive molds of the design and to pattern devices on 22mm x 40mm glass cover slips. The hydrogel reservoir had dimensions of 6.5 x 6.5-mm and a height of approximately 2-mm. Prior to adding a hydrogel to the device, the reservoir was filled with 5M sulfuric acid, washed with distilled water, and incubated in dilute type I collagen (20 μg/mL) to facilitate hydrogel attachment to PDMS (37). The devices were then sterilized using short wavelength UV prior to channel seeding.

ii. Cell culture

Normal human astrocytes (NHA) (Lonza) were thawed at passage 5 and cultured for 10 days in astrocyte growth medium (AGM) (Lonza) prior to seeding in the microfluidic device. Human Coronary Arterial Smooth Muscle Cells (HCASMC) (Sigma) were also thawed at passage 5 and cultured in smooth muscle growth medium (Sigma) until confluency, then passaged and cultured in 6 well plates using smooth muscle cell differentiation medium (Sigma) for 10 days prior to vessel fabrication. Additionally, human cerebral microvascular endothelial cells (HCMEC/d3) received at passage 19 (gifted from Dr. Robert Nagele’s laboratory) were cultured and expanded on tissue culture plates coated with 1% gelatin in EGM-2 modified with CD lipid concentrate and HEPES buffer according to a previously described protocol (38).

iii. In Vitro vessel fabrication

Supplemental Figure 1 provides a visual description of the fabrication process. Briefly, NHA were seeded at a density of 1 million cells per mL in a 10 mg/mL collagen, 1.33 mg/mL hyaluronan (HA) and 1 mg/mL Matrigel hydrogel formulation used in a previous study (39). After injecting the gel directly into the reservoir, an 18-g needle coated with 0.1% Bovine Serum Album (BSA) (Sigma) was inserted into the device through the 18-g needle guide. After waiting 20 minutes to allow for gel polymerization, the needle was pulled to create a cylindrical void, and AGM was added through Port 1 to maintain cell viability. HCASMC were then seeded into a 10 mg/mL collagen and 1 mg/mL Matrigel composite hydrogel at a density of 1 million cells per mL. The AGM was aspirated prior to injection of the hydrogel through Port 3, and a 20-g needle coated in 0.1% BSA in PBS was inserted inside the void lumen using the 20-g needle guide. The 20-g needle was then removed, leaving a final cylindrical void and surrounding annulus. HCMEC/d3 were resuspended in EGM-2 at a density of 5 million per mL. 15 µL of the HCMEC/d3-containing solution was injected into the channel through Port 1 and incubated for 10 minutes, yielding a seeding density of approximately 150,000 cells per cm^2. This process was repeated for an additional 10 minutes after inverting the device to assure uniform lumen coverage throughout the channel. Silicone grease was used to close the 18-g needle guide and Port 2. Port 2 was blocked to increase the length of the recirculation zone along the cell-seeded channel by effectively closing the non-cell seeded branch of the bifurcation. Devices were left in static conditions for 2 days submerged in EGM-2 to ensure cell spreading and viability prior to exposure to flow or static conditions. A total of 29 vessels were fabricated using this method (three for flow validation, six for proliferation assays and viability assays, five for immunohistochemistry, and nine for permeability testing).

iv. Computational fluid dynamics

A computational fluid dynamics (CFD) model was used to predict the flow fields present in the 3D vessels patterned within the microfluidic devices. Prior to the application of flow, brightfield images were acquired of the vessels and used to generate a SolidWorks model that was imported into a commercial finite volume code (Star-CCM+) and discretized by a polyhedral mesh. The maximum flow rate of the peristaltic pump used in our experiments was 4.5 mL/min, so the maximum Reynolds number within the vessels was calculated to be 191. Thus, the flow was laminar in its entirety and there was a sufficient entrance length between Port 1 and the bifurcation to allow for the flow to become fully developed prior to reaching the bifurcation. Furthermore, the Reynolds number necessitated inertial terms in the constitutive flow equation:

$$\rho(\vec{v}\cdot\nabla\vec{v}) = -\nabla \mathrm{p} + \mu\nabla^2\vec{v} \qquad (1)$$

where ρ is the fluid density (kg/m^3), $\vec{v}$ is the fluid velocity vector (m/s), p is the fluid pressure (Pa), and μ is the dynamic viscosity (Pa-s). Additional prism layers were defined in the mesh along the wall boundary to ensure that the near wall effects were adequately resolved. The input flow rate was applied as a velocity boundary condition at Port 1. The gauge pressure at the 20-g needle guide was set to zero, since this provided the outlet for the flow. No-slip boundary conditions were applied at the walls and at Ports 2 and 3 and the 20-g needle guide (locations blocked with silicone grease) to set the velocity to zero at these boundaries. The simulation was run until the solution converged using a steady-state solver.

Disturbed flow was defined by the disruption of a parabolic velocity profile characteristic of fully developed flow and the presence of a recirculation eddy caused by the separated flow. In the computational simulations, the eddy occurred on the near side of the cell-seeded vessel directly downstream of the bifurcation. The location along the wall where the wall shear stress was equal to zero was designated as the stagnation point of the flow. The computational model determined the flow rate that assured the location of the stagnation point was consistent for all geometries, in order to create a reproducible flow field.

v. Micro-particle image velocimetry flow validation

Micro-particle image velocimetry (μPIV) was used to validate the CFD model for three independent channels and to characterize the flow regimes present in these channels. Vessels were perfused with steady state flow by a syringe pump (Kent Scientific) at the flow rates determined by the computational model for their individual geometries. These magnitudes ranged from 4 mL/min to 4.5 mL/min. Polyethylene microspheres labeled with Nile Red (Peak excitation: 640nm; mean diameter 1.95 μm; Spherotech Inc.) were suspended 1:500 in PBS containing 0.1% Triton X-100 to prevent bead aggregation and illuminated and visualized with a dual pulse Nd:YAG laser (125mJ/pulse, 15 Hz, 532 nm; Dantec Dynamics). The pulse width of the lasers was set to 100 ns and the illumination set at a frequency of 0.1 Hz for two seconds (20 individual velocity measurements). Particles were visualized with 10x objective on a Nikon Ti-E inverted microscope, where the focal plane was set to the channel's midpoint. Images were captured using a double-frame CCD camera (FlowSense EO, Dantec Dynamics). Velocity contours were calculated in Dynamic Studio (Dantec Dynamics) using an adaptive PIV algorithm. Velocity contour plots were generated in MATLAB by taking the mean of the 20 velocity measurements. In order to calculate the shear stress at points along the vessel wall, a second order polynomial was fit to the velocity in the boundary layer, and the slope of that function at the wall was calculated.

vi. Flow control

To apply flow to vessels over a 24-hour timespan, a custom peristaltic pump system was built using an Arduino-based control system. A peristaltic motor (Welco) was controlled by an Arduino Uno (Arduino) and a motor board (Ada Fruit). A Sensiron flow sensor was used in-line of the perfusion system to monitor the applied steady flow rate. System schematics are shown in Supplemental Figure 2. The code to control the pump was written and compiled in Arduino IDE (Arduino) using open source libraries available within the IDE (the code is available upon request). To minimize pulsations in the system, a dampener was placed in series with the vessel.

vii. Immunocytochemistry

Four vessels were fabricated using the previously described method. After two days in static culture following cell-seeding, the vessels were either left in static conditions or perfused for 24 hours. Upon completion of the experiment, vessels were fixed in 4% paraformaldehyde (Alfa Aesar) for 30 min at room temperature. Following fixation, the top layer of the microfluidic device was separated using a razor blade, and the hydrogel was then removed from the device. Immunofluorescence was then performed after blocking in 3% BSA for 30 minutes at room temperature and incubating overnight at 4 C in a primary antibody for either zonula occludin-1 (ZO1) (1:250, Cell Signaling Technology, Product 8193), claudin-5 (1:250, Invitrogen, Product 35-2500), occludin (1:250 Invitrogen, Product 71-1500), glial fibrillary acidic protein (GFAP) (1:100, Santa Cruz, Product sc-166481), or alpha smooth muscle cell actin (1:100, ThermoFisher, Product 41-9760-80). Gels were then washed three times with PBS for 5 minutes and incubated in the appropriate secondary antibody (1:500, Santa Cruz, assorted), 1:500 Hoechst (Sigma), and FITC-phalloidin (Sigma, Product P5282) for 1h at 37 C. Confocal stacks were acquired using a Nikon A-1 confocal scanning microscope.

viii. Permeability testing

Nine vessels were used to quantify the permeability of the vessels following perfusion or static culture. At the completion of the 24-hr experiment, the microfluidic devices were placed on the stage of an inverted epifluorescent (Nikon Ti-E) and perfused with 4 kDa FITC-dextran (Sigma) at a flow rate of 10 μL/min using a linear syringe pump over the span of 10 minutes. This flow rate was chosen to avoid any flow separation and assure fully developed flow throughout the channel and to maintain consistency with previously described permeability assays (22). Images were taken at 30-s intervals and then imported into ImageJ for analysis. The permeability coefficient was determined using the following equation (40):

$$P = \frac{di}{dt}\frac{r}{2I_0} \tag{2}$$

Where $\frac{di}{dt}$ is the change in florescent intensity of the region of interest outside the lumen, r is the lumen radius (472 μm) and I_0 is the maximum intensity in the lumen during the test. Permeability was measured at three separate locations corresponding to fully developed flow, near side wall disturbed flow (separated flow), and far side disturbed flow (impingement flow) (designated as I, II, and III).

ix. Cell proliferation assays

Three additional vessels were constructed for proliferation assays, which were based in part on a previous study (4). Briefly, vessels were perfused for 12 hours with EGM-2 using the peristaltic pump and then exposed to 10 μM Bromodeoxyuridine (BrdU) (Alfa Aesar) for the remaining 12 hours. Devices were then briefly washed in PBS and fixed in 4% v/v paraformaldehyde for 30-min at room temperature, quickly washed in PBS, and then permeabilized with 0.2% Triton x100 in PBS for 20 min at room temperature. DNA hydrolysis was performed by removing the hydrogels from the devices and soaking them in a solution consisting of 4 units per mL Turbo DNAse (Thermo fisher) and 0.1 mL DNAse Buffer (Thermo fisher) in PBS for 1 hour at 37C. Gels were washed with PBS then incubated overnight at 4 C with 0.8 μg/mL PE-labeled anti-BrdU (Biolegend) and 1% BSA in PBS. Gels were then counter stained with 1 μg per mL Hoechst for 45 minutes at 37C. In ImageJ, thresholding was used to isolate nuclei prior to using watershedding to isolate individual cells. The ImageJ cell particle counter was used to count the number of nuclei present at three regions of interest in both the disturbed (at the stagnation point) and fully developed regions. In the disturbed region, n = 316-432 Hoechst-positive nuclei were counted. In the fully developed region, n = 261-340 nuclei.

x. Viability assays

Additional vessels were fabricated for viability experiments. Viability was assessed using a Live/Dead kit (Biotium) consisting of calcein AM (2 μM) and ethidium homodimer (4 μM). Vessels were again incubated in static conditions for two days prior to application of flow for 24 hours (controls remained in static conditions for those 24 hours), and then removed from the flow setup, rinsed with PBS, and incubated for 45 minutes in the staining medium prior to imaging. ImageJ was used to calculate the number of live and dead cells in three different regions for each vessel (three vessels were used for both flow and static conditions).

xi. LifeAct transfection

P3 HCASMC cultured in SMC growth medium (Cell Applications) were transfected with RFP LifeAct lentivirus (Ibidi) at a MOI of 2.5. Following 48 hours of incubation with the virus RFP positive cells were selected by adding 5 mg/mL Polybrene until only transfected cells remained attached to the culture plate. Additionally, HCMEC/D3 cells were incubated with lentiviral particles containing copGFP using a MOI of 1 overnight. The cells were then washed and incubated in EGM-2 and exposed to 10 mg/mL puromycin until ~90% of adhered cells expressed GFP. Transfected cells were then cultured and used for experiments as needed.

xii. Dynamic mechanical testing

Hydrogels with and without astrocytes were polymerized within the central reservoir of the microfluidic devices, and then removed after two days in static culture and transferred to a compression platen for axial dynamic mechanical testing (EZ-SX, Shiamadzu). Due to the fixed geometry of the microfluidic reservoir, all hydrogels had dimensions of 1-cm width, 1-cm length, and 1.6-mm height. The hydrogels were compressed at a frequency of 0.5 Hz between 0 and 15% strain in an unconfined configuration. The complex modulus was calculated by the ratio of the maximum stress and maximum strain. The phase shift between the stress and strain waveforms was used to determine the loss angle, and consequently the storage and loss modulus of the hydrogels. Three samples were tested for both cellular and acellular conditions (six total samples).

xiii. Astrocyte message level quantification

After perfusion, hydrogels were removed from the microfluidic device and cut into regions representative of disturbed, impingement, and fully developed regions. mRNA from the astrocytes was isolated using PicoPure RNA Isolation kits (Thermo Scientific) and reverse transcribed to cDNA using qScript (Quantabio). Quantitative PCR was then performed with SYBR Green reagents, with the primers given in Table 1 used to amplify targets. Tests were conducted in triplicate for each region.

Primer	Forward Sequence	Reverse Sequence
NONO	**GTGTAGCGTCGCCGTTACTC**	**CCTTCATTTTGGCTGCTGGC**
VEGF	**GACATTGCTGTGCTTTGGGG**	**AAGGGGAGCAGGAAGAGGAT**
HIF1a	**TGGCAACCTTGGATTGGATGGA**	**CCGTCCCTCAACCTCTCAGT**
GFAP	**CAAAAGCACCAAAGACGGGG**	**GAGGCTCACTCCCTGTCAAG**

Table 1: Primer sequences for astrocyte qRT-PCR

Message levels were double normalized to Non-POU domain-containing octamer-binding protein (NONO) from a collagen-only sample. Relative expression was quantified as $2^{-\Delta\Delta C_T}$ where C_T is cycles to threshold. Data are presented as the averaged fold change of collagen/HA gels compared to collagen only gels.

ix. Alignment quantification

Endothelial cell alignment was quantified by transforming the spatial information from the phalloidin signal into the frequency domain using a fast Fourier transform (FFT) calculated by ImageJ as described in a previous publication (41). A Gaussian curve was fit to the frequency data, and the half-width of the curve was calculated for cells exposed to fully developed and disturbed flow. This process was repeated for three separate 100 x 100-μm sections from a single immunofluorescence image.

x. Statistical analysis

The open source statistics package, R, was used to perform all statistical calculations. Pairwise t-tests were used to compare measurements of permeability coefficients and positive BrdU staining. Shapiro-Wilk tests were performed prior to the t-tests, and p-values were found to be greater than 0.05 for all datasets, verifying the normality assumption for the data. Each comparison was made for sample numbers greater than or equal to 3, and $p < 0.05$ was considered significant.

Results

i. Fabrication and characterization of a 3D in vitro model of a cerebral bifurcation

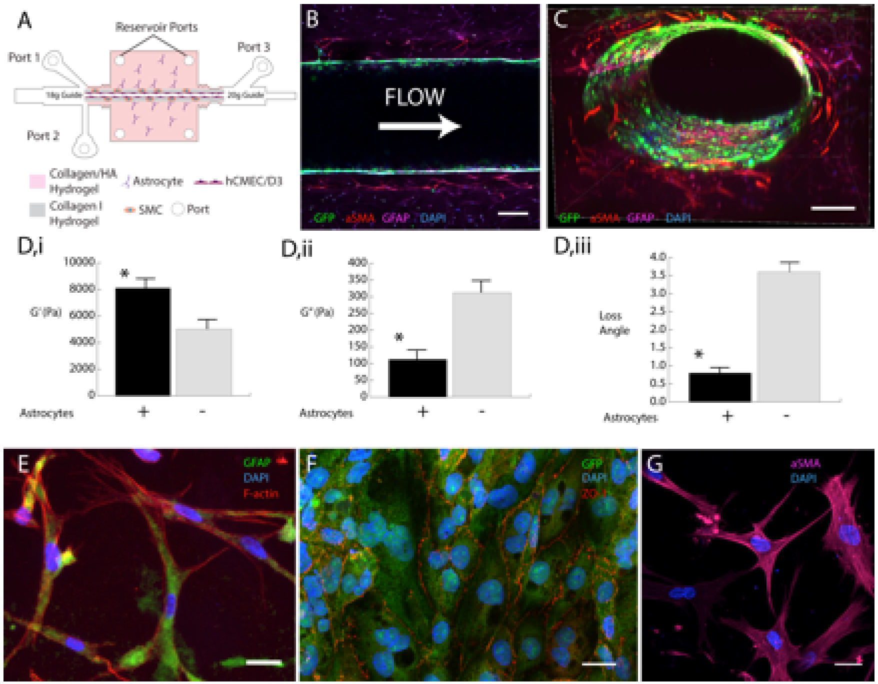

Figure 1. Fabrication of a 3D cerebral bifurcation model. A) Schematic of the microfluidic device showing the location of the ports and the needle guides used to create the layered cell-seeded vessel, B) Cross-section of the vessel at its midpoint with GFP-labeled endothelial cells (green), LifeAct-RFP smooth muscle cells (red), and GFAP-positive astrocytes (magenta). scale = 100 μm. The arrow indicates the flow direction. C) 3D reconstruction of vessel scale = 100 μm. D) Storage moduli (i), loss moduli (ii), and phase angle (iii) of hydrogels seeded with and without astrocytes. (n = 3) E) Astrocytes labeled with DAPI (blue), phalloidin (red), and anti-GFAP (green). F) GFP-labeled endothelial cells (green) exhibiting ZO-1 at cell-cell junctions (red). G) α-SMA-positive smooth muscle cells. Scale bars are 25μm in E, F, and G.

A microfluidic device was designed to apply bifurcation flow profiles to a 3D model of a cerebral artery, consisting of an endothelial intima and a smooth-muscle containing media layer surrounded by astrocytes. The device schematic in Figure 1A indicates the location of a 944-μm diameter endothelialized lumen surrounded by a smooth muscle cell-containing annulus with an outer diameter of 1.2 mm in a hydrogel seeded with astrocytes. To induce flow separation, defined as a disruption of a fully developed boundary layer, the flow inlet and cell-seeded vessel were offset by 45 degrees. Figure 1B shows a cross-section at the midpoint of the channel after 3 days in culture, indicating a confluent monolayer of GFP-positive endothelial cells (hCMEC/D3), an annulus of LifeAct-RFP expressing smooth muscle cells (hCMASMC), and an outer hydrogel of glial fibrillary acidic protein (GFAP)-positive astrocytes (NHA). Figure 1C provides a 3D reconstruction of the co-culture vessel, further verifying the stable stratification of the three cell types within the model.

Preliminary flow tests in the microfluidic device revealed that astrocytes were needed within the hydrogel to prevent collapse of channels exposed to high flow rates. Given that previous studies have demonstrated that embedding astrocytes within collagen/hyaluronan composite matrices affects their viscoelastic properties (42), we conducted dynamic mechanical testing of hydrogels with and without astrocytes. The compression testing indicated that hydrogels seeded with astrocytes featured an increased storage modulus (Fig. 1D,i), decreased loss modulus (Fig. 1D,ii), and reduced phase angle (Fig. 1D,iii) compared to acellular controls. This finding is consistent with our previous result that astrocytes alter the mechanical properties of a constrained collagen/hyaluronan hydrogel by exertion of cell-generated forces on the matrix (42). Hence, astrocytes were required in the model not only to mimic the glial cells surrounding cerebral vasculature in vivo, but also to sustain forces exerted by high Reynolds number flow.

Immunofluorescence using cell type-specific markers verified that the three cell types retained their phenotype after several days in the co-culture. Figure 1E shows the astrocytes within the outer hydrogel: the cells **attached to** the extracellular matrix and exhibited positive staining for GFAP, a marker of astrocyte activation. Figure 1F provides an image of the confluent endothelial monolayer lining the vessel lumen. After the application of flow, the endothelial cells exhibited localization of zonula occuldin-1 (ZO-1) to the cell-cell junctions, indicative of tight junction formation. Finally, the smooth muscle cells within the annulus maintained their phenotype, as evidenced by positive staining for α-smooth muscle cell actin (α-SMA) (Fig. 1G).

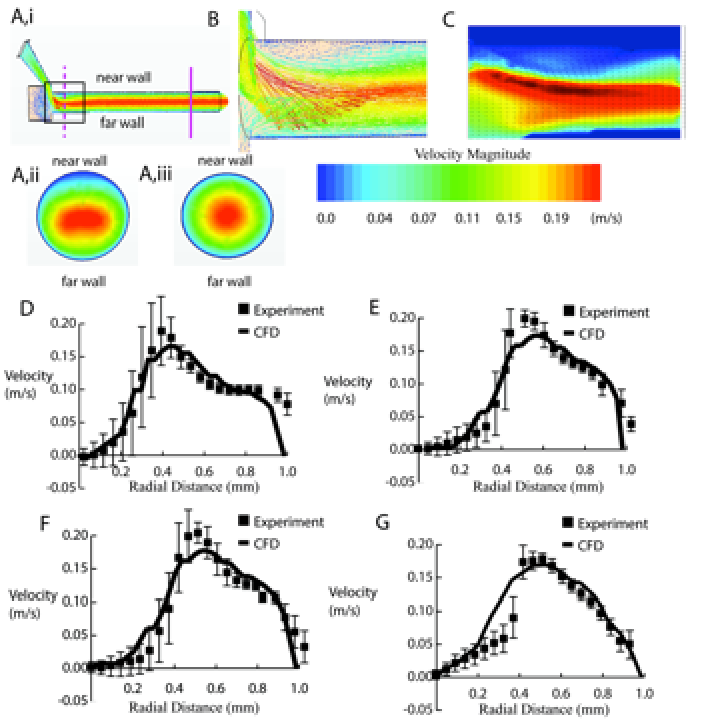

Figure 2. Flow characterization of the bifurcation. A,i) Velocity contour plot generated with the CFD software using a flow rate of 4 mL/min. A,ii) A radial velocity plot in the disturbed region (purple dotted line) and A,iii) fully developed region (purple solid line). B) Velocity contour plot within the boxed region of panel A. C) Velocity contour plot measured with microparticle image velocimetry and processed with a MATLAB code. D) Velocity profile along the channel radius at x= 0.18 mm E) x= 0.33mm, F) x= 0.55mm and, G) x= 1 mm. Error bars indicate the standard deviation between 20 frames.

ii. Flow characterization within the microfluidic device

A 3D computational fluid dynamics (CFD) model was constructed to characterize the flow within the microfluidic device and to determine the flow rate required to cause flow separation along the cell-seeded vessel. A brightfield image of the channel geometry was imported into SolidWorks, discretized, and meshed using a commercial CFD code (Star CCM+). The CFD model predicted flow separation at the near wall of the cell-seeded vessel for an input flow rate of 4 mL/min (Fig. 2A,i). At this location, the velocity profile was no longer parabolic and a recirculation eddy was present. The flow reattached to the wall 2.2-mm downstream of the vessel inlet, as evidenced by the onset of constant wall shear stress and a fully developed velocity profile. Radial velocity plots in the disturbed (Fig. 2A,ii) and fully developed (Fig. 2A,iii) regions indicated the flow separation caused by the bifurcation. A velocity contour at the bifurcation (Fig. 2B) further exhibited the asymmetric flow profile and separation from the near wall of the cell-seeded vessel.

In order to validate the computational model, microparticle image velocimetry (μPIV) was used to quantify the velocity profile within the vessel. Flow was applied at the 4-mL/min rate used in the computational model, and the velocity contour was measured within the cell-seeded vessel. As Figure 2C indicates, μPIV demonstrated a similar region of separated flow at the inlet of the cell-seeded vessel as the computational model (Fig. 2B). At four distances from the inlet of the cell-seeded vessel (x = 0.28 mm, 0.33 mm, 0.55 mm, and 1 mm), the velocity profiles predicted by the computational model were compared to the measurements from the μPIV measurements (Fig. 2D-G). The plots indicate close agreement between the predicted velocity distributions and those measured by μPIV. For most data points, the computational value falls within one standard deviation of the experimental measurement, with the exception of the contour at x = 1-mm (Fig. 2G) where the computational model overestimates the velocity measured experimentally at radial distances varying from 0.2 to 0.5-mm. A possible cause for this discrepancy is small variations in channel geometry caused by perfusion, since the computational model is based on the channel geometry in static conditions. To interrogate the effect of perfusion on channel geometry, the deformation of the channel walls was measured during the application of 8 mL/min flow, which was the maximum flow rate applied by the pump, and found to increase by 0.5 +/- 0.01% on average along the channel length (measured in three locations for three separate channels). The deformed geometries were then input into the computational model to determine its effect on predicted velocity distribution at x = 1-mm. As Supplemental Figure 3 indicates, changes to the wall geometry caused by perfusion do not substantially alter the wall shear stress along the channel, suggesting that another factor is likely responsible for the discrepancy in Figure 2G. Nonetheless, the maximum velocity and asymmetry of the distributions were consistent between calculated and experimental data, validating the accuracy of the computational model.

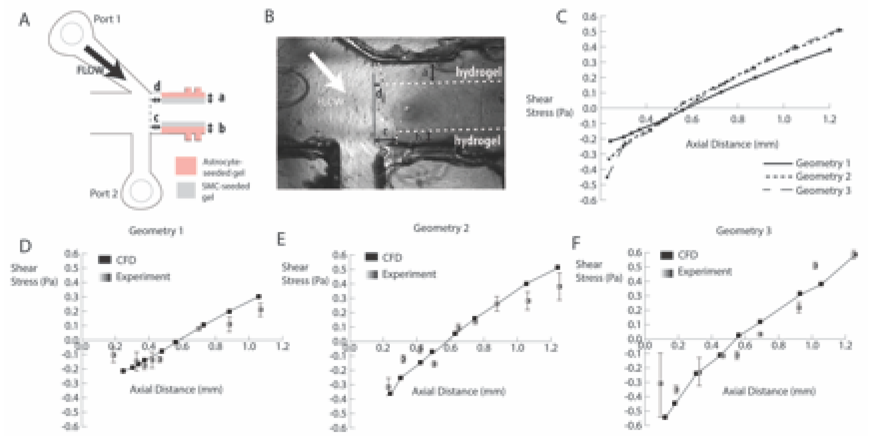

Figure 3. Generalized model to account for geometric variation: A) Schematic of the bifurcation detailing the parameters used to quantify differences in vessel geometry. B) A brightfield image indicating the location of these parameters in a sample vessel. C) Wall shear stress profiles generated with CFD for three different geometries and flow rates varying from 4-4.5mL/min. D-F) comparison plots between the experimental and measured wall shear stress (WSS) profiles along a 1.2-mm length of the near wall of the disturbed region for geometries 1,2 and 3. Error bars indicate the standard deviation of 20 measurements.

iii. Generalized model to account for geometric variation

Having demonstrated the efficacy of the computational model to predict velocity distributions within the device, additional work was conducted to assure that reproducible flow profiles could be applied to multiple channels despite small differences in channel geometry caused by the placement of needles within the hydrogel. Therefore, in order to create a repeatable system for cell studies, an approach was developed to normalize the flow fields for varying geometries. Specifically, the computational model was used to determine the flow rate required to fix the location of the flow stagnation point (where wall shear stress was equal to zero on the near side wall) at the same distance from the inlet regardless of the channel geometry. Four parameters were used to describe the channel geometry prior to application of flow, depicted in Figures 3A and 3B. These parameters provided insight into the position of the hydrogel within the microfluidic device in order to account for slight differences in the placement and orientation of the cell-seeded vessels. Parameters A and B indicated the extent to which the channel was centered within the device, and Parameters C and D described the lateral placement of the hydrogel. Table 2 summarizes the values of these four parameters for three different channel geometries (Geometry 1, Geometry 2, and Geometry 3).

Geometry	Parameter A (mm)	Parameter B (mm)	Parameter C (mm)	Parameter D (mm)
1	**0.38**	**0.31**	**0**	**0**
2	**0.40**	**0.30**	**0**	**0**
3	**0.47**	**0.24**	**0.1**	**0**

Table 2: Geometry parameterization of the channels

For the three geometries, the average and standard deviation of the stagnation point was predicted to occur at 0.543 mm +/- 0.029 mm and the length of the disturbed region was 2.17 mm +/- 0.44 mm for flow rates varying from 4 to 4.5 mL/min. The predicted shear profiles along the near-side wall of the vessel are shown in Figure 3C. Due to the changes in flow rate, the average shear stress among the three geometries in the fully developed region downstream of the bifurcation was 0.835 Pa +/- 0.056 Pa, which is consistent with physiological levels for the middle cerebral artery (43). μPIV was used to validate the shear stress profiles for the three geometries along a 1.2-mm-length of the channel adjacent to the bifurcation on the near wall (Figs. 3D-F). The plots show close agreement between the predicted shear stress distributions and those measured by μPIV. Importantly, the distributions all indicate substantial recirculation zones and a similar stagnation point for all three geometries. These results verify that the stagnation point of the flow can be fixed regardless of small changes to vessel geometry, allowing for a reproducible flow environment for studying the endothelial response in multiple samples**.**

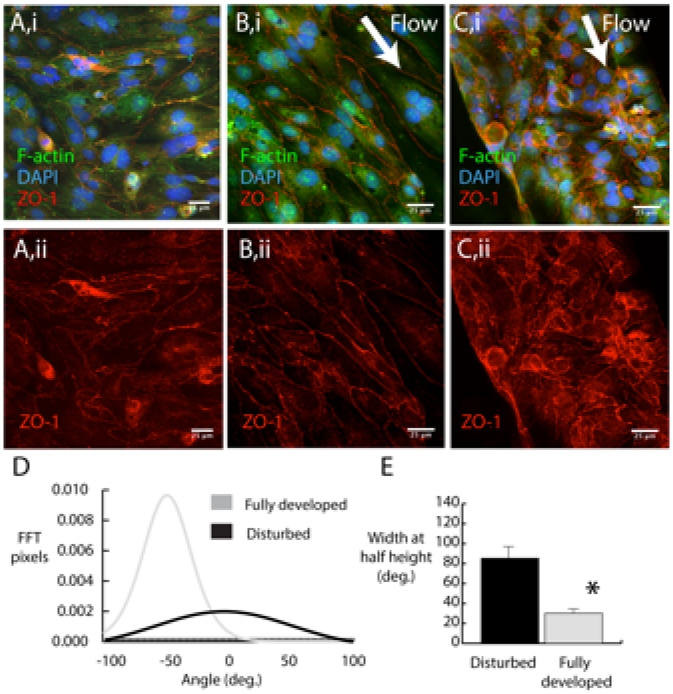

Figure 4. Effects of disturbed flow on endothelial cells tight junctions: A-C) Composite images of ZO-1 (red), DAPI (blue), and phalloidin (green) (i) and with ZO-1 isolated (ii) of the endothelial cells along the near side wall in static conditions (A) and in perfused channels at the fully developed (B) and stagnation point of the disturbed region (C). Scale for A-C: 25 μm D) Gaussian distribution of the actin fibers fitted to results of FFT analysis. E) Width at half height of the distributions for disturbed and fully developed regions. * $p < 0.05$.

iv. Effects of disturbed fluid flow on endothelial tight junctions and morphology

Having demonstrated that disturbed flow could reproducibly be applied to the vessels despite inconsistencies in channel geometry, experiments were conducted to assess the effect of disturbed flow on the integrity of tight junctions within the endothelial monolayer. In vitro vessels were either exposed to flow for 24-h with flow rates that caused flow separation at the location of the bifurcation, or cultured in static conditions as an additional control. Imaging of the monolayer exposed to static conditions revealed that ZO-1 was not fully localized to cell-cell junctions (Fig. 4A,i-ii). In contrast, endothelial cells exposed to fully developed flow exhibited ZO-1 localization to the cell-cell junctions (Fig. 4B,i-ii). In the disturbed region, images of the endothelium at the stagnation point indicated a disorganized monolayer with substantially less ZO-1 staining at the junctions (Fig. 4C,i-ii). FFT analysis suggested that the cells in the fully developed region were significantly more aligned in the direction of flow than cells in the disturbed region (Fig. 4D-E). To provide further evidence of tight junction formation and disruption in these different regions, vessels were also treated with antibodies for claudin-5 and occludin, two additional markers for the tight junctions characteristic of the BBB. These images are provided in Supplementary Figure 4.

v. Effects of disturbed fluid flow on endothelial cell proliferation and viability

As shown in Figure 4, the endothelium in the disturbed region appeared to have a higher cell density than the region in the fully developed region downstream of the bifurcation. To determine whether disturbed flow augmented proliferation in the disturbed region, a BrdU assay was conducted to compare the number of cells in S-phase between the disturbed and fully developed regions. Based on channel geometries, flow rates were chosen to match the wall shear stress distributions used in the immunofluorescence and permeability assays and applied for 24-h. After 12-h, BrdU was added into the perfusing medium. Imaging of the fully developed region showed few BrdU-positive nuclei (Fig. 5A) In contrast, the disturbed region (Fig. 5A) exhibited an increased number of BrdU-positive nuclei (and higher number of nuclei overall) at the location of the stagnation point of the near wall (Fig. 5B). Quantification of the disturbed and fully developed regions indicated a significant increase in the number of BrdU-positive cells. In the disturbed region: 65% of cells were in S-phase compared to only 3% in the fully developed region (Fig. 5C). This result is consistent with previous studies that found increased endothelial proliferation is associated with barrier breakdown (44).

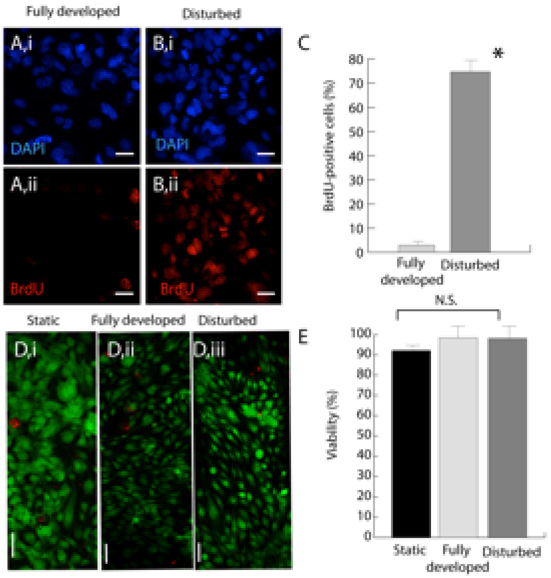

Figure 5. Effects of disturbed flow on endothelial cell proliferation and viability: A-B) DAPI (i) and BrdU (ii) staining of the endothelial lumen for fully developed (A) and disturbed (at the stagnation point of the near wall) (B) regions. Scale bars = 25μm. C) Percent of BrdU-positive nuclei (n=3). *indicates $p < 0.05$. D) Live (green) / Dead (red) assay for cells exposed to static (i), fully developed (ii), and disturbed (iii) flow. Scale bars = 100 μm. E) Quantification of Live/Dead assay for three different vessels for each condition (n = 3). N.S indicates no significant difference.

To verify that endothelial cell viability was not affected by the different flow regimes, a Live/Dead assay was conducted for static, disturbed, and fully developed conditions. Across all conditions, the viability exceeded 92% regardless of the shear stress exerted on the endothelium. Furthermore, there were no significant differences in the amount of viable cells between static (Fig. 5D,i), fully developed (Fig. 5D,ii), and disturbed (Fig. 5D,iii). Figure 5E provides a summary of the quantified data, indicating no significant difference in viability between the different flow regimes. These results indicate that although cells in the disturbed region proliferated at a higher rate, they remained viable during the flow experiments.

vi. Quantification of vessel permeability and endothelial-mural/endothelial-glial interaction

Permeability testing provided a quantitative means to assess the integrity of the barrier in response to varying flow regimes. Devices were perfused with dextran to quantify barrier integrity after 24-h of perfusion. The permeability coefficient was measured at the fully developed region downstream of the bifurcation (I) and at the near wall (where flow separates) (II) and far wall (III) adjacent to the bifurcation in the area of disturbed flow. Figure 6A provides an image of a vessel being perfused with dextran to assess barrier permeability and denotes the three regions where the permeability was measured. Figure 6B indicates that the permeability is significantly higher in not only the near wall of the disturbed region (II) compared to the fully developed region (I), but also at the far wall of the disturbed region (III). At this location, the vessel wall experiences impingement flow: the shear stress was elevated compared to other regions of the vessel (1.4 Pa +/- 0.22 Pa) and the shear varied along the axial direction of the vessel. This result supports previous studies linking impingement flow (45) and high shear stress (46) to vascular dysfunction in the brain. In order to verify that the increased dextran transport adjacent to the bifurcation was not due to leakage from the side of the hydrogel, the gradient of fluorescence intensity was graphed in both the axial and radial direction for the disturbed region. Supplementary Figure 5 indicates that the fluorescence intensity gradient along the axial direction is relatively constant compared to the radial direction, suggesting that the transport of dextran into the surrounding hydrogel is primarily through the cells exposed to disturbed flow. Overall, these permeability tests verify the results of the tight junction staining that suggest disturbed flow disrupts barrier function.

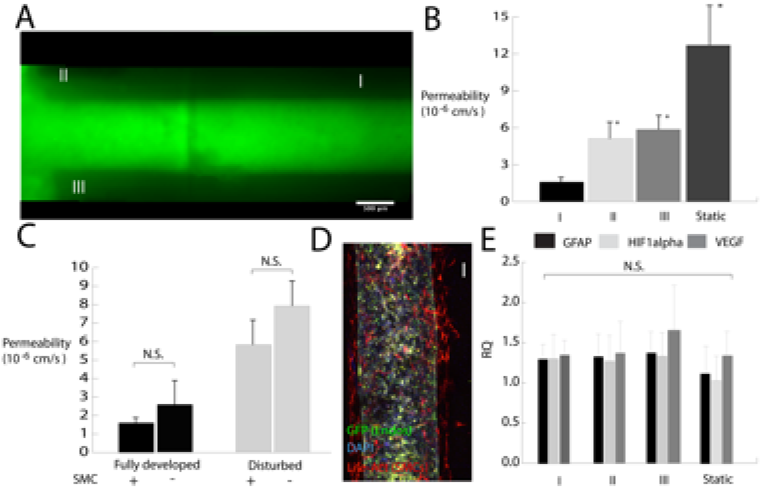

Figure 6: Effect of disturbed flow on vessel permeability and smooth muscle cell and astrocyte interaction. A) An image of dextran perfusion indicating the location of permeability measurements: I) Fully developed, II) Disturbed on the near side wall (separated flow), III) Disturbed on the far side wall (impingement flow). B) Quantification of the permeability constant at these three regions and a static control. (n = 3) C) Quantification of permeability coefficients for vessels lacking smooth muscle cell incorporation. (n = 3) D) A representative image of smooth muscle cell orientation along the endothelialized vessel. E) Relative gene expression of GFAP, HIF1alpha, and VEGF of astrocytes isolated from regions adjacent to endothelial cells exposed to fully developed (I), disturbed (II), impinged flow (III), and static conditions. (n = 3) * indicates $p < 0.05$. N.S indicates no significant difference

In order to probe endothelial-mural crosstalk, permeability tests were repeated on vessels with smooth muscle cells removed from the annulus. Given the effect of mural cells on regulation of vascular tone (47), lipid absorption (48), and small GTPase signaling within endothelial cells (49), these experiments interrogated whether smooth muscle cells also influenced the response of the BBB to altered shear stress. Figure 6C indicates that the absence of smooth muscle cells did not cause a significant effect in the permeability of the endothelium in the disturbed and fully developed regions. Additional imaging experiments were conducted to determine if the spatial organization of the smooth muscle cells varied along the vessel (Fig. 6D). Quantification of the distance between smooth muscle cell nuclei and the endothelial lumen indicated no significant difference between disturbed and fully developed regions.

Astrocytes in regions adjacent to the three flow regimes (I: fully developed, II: disturbed, and III: impinged) were isolated and lysed following application of flow to determine whether glial cells mediated barrier disruption by undergoing activation or increasing gene expression of paracrine factors known to cause barrier breakdown. Although gene expression does not elucidate the underlying mechanisms regulating the response of astrocytes to their environmental factors, this assay provides insight into whether the flow regime affected the astrocyte cell response. Message level quantification indicated no significant difference in the production of GFAP, which is indicative of glial activation, or in the production of paracrine factors VEGF and HIF1α, which are known to modulate vascular integrity and function. These results verified that astrocytes surrounding the endothelium exposed to different flow regimes did not affect barrier integrity by altering their gene expression.

Discussion

The results presented here contribute to the growing evidence that fluid shear stress modulates the integrity of the BBB. Whereas a previous study from one of our groups demonstrated the protective effects of low levels of shear on the BBB (22), here, our findings indicate that shear stress altered by disturbed flow has the opposite effect. Endothelial cells within the region of separated flow exhibit altered morphology, increased permeability, and higher proliferation rates compared to cells in the fully developed flow region downstream of the bifurcation. Although previous studies have identified similar consequences of disturbed flow in other parts of the body (50), the current findings show that vasculature in the brain is also impacted by the altered shear stress exerted by separated flow. Because the barrier function of brain vasculature is more vital than vasculature in other regions of the body due to the inflammation caused by the leakage of plasma components into the brain parenchyma, these results underscore the impact of disturbed blood flow in the brain. Additionally, given that recent studies (51, 52) have found transcellular breakdown precedes the paracellular transport measured here, the effect of disturbed flow on the barrier may be even more pronounced than our experiments indicate.

The results also demonstrate that the cerebral bifurcation model provides a robust platform to study the response of brain vasculature to complex fluid mechanics. Unlike previous in vitro models designed to exert disturbed flow on endothelial cells, the current model preserves the three-dimensionality of the in vivo environment and incorporates both mural and glial cells in the surrounding hydrogel. Although our results suggest that smooth muscle cells and astrocytes do not modulate the endothelial response to disturbed flow, these findings do not contradict previous findings on the importance of endothelial-mural and endothelial-glial crosstalk. Rather, the results indicate that the endothelium modulates tight junction integrity in response to fluid shear stress independent of other cell types, which is consistent with a previous finding that cerebral endothelial cells exposed to shear stress form tight junctions in the absence of astrocytes (22). Although the model mimics certain aspects of in vivo vasculature that have yet to be incorporated in vitro, it does not fully recreate the in vivo microenvironment and focuses on a rather short (24-hour) time frame. There are differences in both the ECM content (brain tissue contains minimal fibrillar collagen type I) and a lack of cell types including microglia, pericytes, and macrophages that could affect the specific range and magnitude of shear stress that causes barrier breakdown in vivo. Furthermore, the current microfluidic device exhibits a fixed bifurcation geometry, since the inlet is offset by 45 degrees, and thus cannot mimic the variability present in cerebral bifurcations. Therefore, future work is required to determine whether barrier function is generally reduced adjacent to bifurcations in the brain or additional factors known to exacerbate the effects of disturbed flow in systemic vasculature (53) also exert the same effect on the blood-brain barrier.

However, despite these differences with in vivo vasculature, a particular advantage of this in vitro model is the use of CFD and μPIV to predict and validate the complex flow fields generated in the device. These methods are vital to assuring consistency between the varying channels, since the fabrication of the cell-seeded hydrogels results in small differences in geometries that affect the flow field. All the geometries tested exhibit a substantial length of flow separation (~ 2 mm) and a region of recirculating flow. Given the 944-μm diameter of the vessel and a cell density measured in the BrdU assay of 182,430 cells/cm^2 +/- 30,230 cell/cm^2 on the near side of the vessel in the disturbed region, approximately 12,000 cells were exposed to separated flow, a sufficient number to conduct future gene and protein expression studies. One potential target for future studies is the effect of disturbed flow on the formation of cerebral aneurysms. Previous studies have demonstrated that most cerebral aneurysms occur at or near arterial bifurcations (24). These locations are most susceptible to the formation of recirculation eddies and separated flow, due to their geometry and the higher Reynolds number of the flow. The increased incidence at bifurcations is readily apparent in the middle cerebral artery: a previous study found that 96/100 middle cerebral artery aneurysms occurred at bifurcations or trifurcations (54). Moreover, factors associated with BBB disruption, specifically MMP9, are also connected with the formation of cerebral aneurysms (55), further linking barrier breakdown to aneurysms. In addition to aneurysm formation, disturbed flow could also contribute to other vascular dysfunction: a recent study of the effects of inhaled anesthetics on BBB breakdown found that endothelial damage was localized to vascular bifurcations (25). Overall, the bifurcation model provides a means to interrogate the role of disturbed flow in the formation and progression of these pathologies.

Conflicts of interest

There are no conflicts to declare

Acknowledgements

The authors would like to acknowledge Dr. Robert Nagele for kindly providing the claudin-5 and occludin antibodies used in the study.

Sources of Funding

This work was supported by NSF Award ID 1728239 (P.A.G.).

Author Contributions

N.B., B.J.D. and P.A.G. performed experiments. N.B., C.Z., and D.W.S. constructed and analyzed the computational fluid dynamics model. N.B., B.J.D., J.S.M., and P.A.G. wrote and edited the manuscript.

Institutional committee

Experiments were approved by the Rowan University Institutional Review Board

References

1. Daneman R, Prat A. The blood-brain barrier. Cold Spring Harb Perspect Biol. 2015;7(1):a020412.
2. McLoughlin A, Rochfort KD, McDonnell CJ, Kerrigan SW, Cummins PM. Staphylococcus aureus-mediated blood-brain barrier injury: an in vitro human brain microvascular endothelial cell model. Cell Microbiol. 2017;19(3).
3. Hersom M, Helms HC, Pretzer N, Goldeman C, Jensen AI, Severin G, et al. Transferrin receptor expression and role in transendothelial transport of transferrin in cultured brain endothelial monolayers. Mol Cell Neurosci. 2016;76:59-67.
4. Chiu J-J, Chien S. Effects of Disturbed Flow on Vascular Endothelium: Pathophysiological Basis and Clinical Perspectives. Physiological reviews. 2011;91(1):10.1152/physrev.00047.2009.
5. Masuda H, Shozawa T, Hosoda S, Kanda M, Kamiya A. Cytoplasmic microfilaments in endothelial cells of flow loaded canine carotid arteries. Heart Vessels. 1985;1(2):65-9.
6. Bharadvaj BK, Mabon RF, Giddens DP. Steady flow in a model of the human carotid bifurcation. Part II--laser-Doppler anemometer measurements. J Biomech. 1982;15(5):363-78.
7. Motomiya M, Karino T. Flow patterns in the human carotid artery bifurcation. Stroke. 1984;15(1):50-6.
8. Davies PF, Shi C, Depaola N, Helmke BP, Polacek DC. Hemodynamics and the focal origin of atherosclerosis: a spatial approach to endothelial structure, gene expression, and function. Ann N Y Acad Sci. 2001;947:7-16; discussion -7.
9. Ting LH, Jahn JR, Jung JI, Shuman BR, Feghhi S, Han SJ, et al. Flow mechanotransduction regulates traction forces, intercellular forces, and adherens junctions. Am J Physiol Heart Circ Physiol. 2012;302(11):H2220-9.
10. Chappell DC, Varner SE, Nerem RM, Medford RM, Alexander RW. Oscillatory shear stress stimulates adhesion molecule expression in cultured human endothelium. Circ Res. 1998;82(5):532-9.
11. Chiu JJ, Wang DL, Chien S, Skalak R, Usami S. Effects of disturbed flow on endothelial cells. J Biomech Eng. 1998;120(1):2-8.
12. Ku DN, Giddens DP, Zarins CK, Glagov S. Pulsatile flow and atherosclerosis in the human carotid bifurcation. Positive correlation between plaque location and low oscillating shear stress. Arteriosclerosis. 1985;5(3):293-302.
13. DePaola N, Gimbrone MA, Jr., Davies PF, Dewey CF, Jr. Vascular endothelium responds to fluid shear stress gradients. Arterioscler Thromb. 1992;12(11):1254-7.
14. Lei M, Archie JP, Kleinstreuer C. Computational design of a bypass graft that minimizes wall shear stress gradients in the region of the distal anastomosis. J Vasc Surg. 1997;25(4):637-46.
15. Tardy Y, Resnick N, Nagel T, Gimbrone MA, Jr., Dewey CF, Jr. Shear stress gradients remodel endothelial monolayers in vitro via a cell proliferation-migration-loss cycle. Arterioscler Thromb Vasc Biol. 1997;17(11):3102-6.
16. Dorland YL, Huveneers S. Cell-cell junctional mechanotransduction in endothelial remodeling. Cell Mol Life Sci. 2017;74(2):279-92.
17. Bell RD, Zlokovic BV. Neurovascular mechanisms and blood-brain barrier disorder in Alzheimer's disease. Acta Neuropathol. 2009;118(1):103-13.
18. Seiffert E, Dreier JP, Ivens S, Bechmann I, Tomkins O, Heinemann U, et al. Lasting blood-brain barrier disruption induces epileptic focus in the rat somatosensory cortex. J Neurosci. 2004;24(36):7829-36.
19. Heinemann U, Kaufer D, Friedman A. Blood-brain barrier dysfunction, TGFbeta signaling, and astrocyte dysfunction in epilepsy. Glia. 2012;60(8):1251-7.

20. Schoknecht K, Prager O, Vazana U, Kamintsky L, Harhausen D, Zille M, et al. Monitoring stroke progression: in vivo imaging of cortical perfusion, blood-brain barrier permeability and cellular damage in the rat photothrombosis model. J Cereb Blood Flow Metab. 2014;34(11):1791-801.

21. Cucullo L, Hossain M, Puvenna V, Marchi N, Janigro D. The role of shear stress in Blood-Brain Barrier endothelial physiology. BMC Neurosci. 2011;12:40.

22. Partyka PP, Godsey GA, Galie JR, Kosciuk MC, Acharya NK, Nagele RG, et al. Mechanical stress regulates transport in a compliant 3D model of the blood-brain barrier. Biomaterials. 2017;115:30-9.

23. Reese TS, Karnovsky MJ. Fine structural localization of a blood-brain barrier to exogenous peroxidase. J Cell Biol. 1967;34(1):207-17.

24. Dashti R, Hernesniemi J, Niemela M, Rinne J, Porras M, Lehecka M, et al. Microneurosurgical management of middle cerebral artery bifurcation aneurysms. Surg Neurol. 2007;67(5):441-56.

25. Acharya NK, Goldwaser EL, Forsberg MM, Godsey GA, Johnson CA, Sarkar A, et al. Sevoflurane and Isoflurane induce structural changes in brain vascular endothelial cells and increase blood-brain barrier permeability: Possible link to postoperative delirium and cognitive decline. Brain Res. 2015;1620:29-41.

26. Galie PA, Nguyen DH, Choi CK, Cohen DM, Janmey PA, Chen CS. Fluid shear stress threshold regulates angiogenic sprouting. Proc Natl Acad Sci U S A. 2014;111(22):7968-73.

27. Nguyen DH, Stapleton SC, Yang MT, Cha SS, Choi CK, Galie PA, et al. Biomimetic model to reconstitute angiogenic sprouting morphogenesis in vitro. Proc Natl Acad Sci U S A. 2013;110(17):6712-7.

28. Grigoryan B, Paulsen SJ, Corbett DC, Sazer DW, Fortin CL, Zaita AJ, et al. Multivascular networks and functional intravascular topologies within biocompatible hydrogels. Science. 2019;364(6439):458-64.

29. Griep LM, Wolbers F, de Wagenaar B, ter Braak PM, Weksler BB, Romero IA, et al. BBB on chip: microfluidic platform to mechanically and biochemically modulate blood-brain barrier function. Biomed Microdevices. 2013;15(1):145-50.

30. Brown JA, Pensabene V, Markov DA, Allwardt V, Neely MD, Shi M, et al. Recreating blood-brain barrier physiology and structure on chip: A novel neurovascular microfluidic bioreactor. Biomicrofluidics. 2015;9(5):054124.

31. Herland A, van der Meer AD, FitzGerald EA, Park TE, Sleeboom JJ, Ingber DE. Distinct Contributions of Astrocytes and Pericytes to Neuroinflammation Identified in a 3D Human Blood-Brain Barrier on a Chip. PLoS One. 2016;11(3):e0150360.

32. Campisi M, Shin Y, Osaki T, Hajal C, Chiono V, Kamm RD. 3D self-organized microvascular model of the human blood-brain barrier with endothelial cells, pericytes and astrocytes. Biomaterials. 2018;180:117-29.

33. Linville RM, DeStefano JG, Sklar MB, Xu Z, Farrell AM, Bogorad MI, et al. Human iPSC-derived blood-brain barrier microvessels: validation of barrier function and endothelial cell behavior. Biomaterials. 2019;190-191:24-37.

34. Cucullo L, McAllister MS, Kight K, Krizanac-Bengez L, Marroni M, Mayberg MR, et al. A new dynamic in vitro model for the multidimensional study of astrocyte-endothelial cell interactions at the blood-brain barrier. Brain Res. 2002;951(2):243-54.

35. Qi Y-X, Jiang J, Jiang X-H, Wang X-D, Ji S-Y, Han Y, et al. PDGF-BB and TGF-β1 on cross-talk between endothelial and smooth muscle cells in vascular remodeling induced by low shear stress. Proceedings of the National Academy of Sciences. 2011;108(5):1908.

36. Robert J, Button EB, Yuen B, Gilmour M, Kang K, Bahrabadi A, et al. Clearance of beta-amyloid is facilitated by apolipoprotein E and circulating high-density lipoproteins in bioengineered human vessels. Elife. 2017;6.

37. Galie PA, Stegemann JP. Simultaneous application of interstitial flow and cyclic mechanical strain to a three-dimensional cell-seeded hydrogel. Tissue Eng Part C Methods. 2011;17(5):527-36.

38. Weksler BB, Subileau EA, Perriere N, Charneau P, Holloway K, Leveque M, et al. Blood-brain barrier-specific properties of a human adult brain endothelial cell line. FASEB J. 2005;19(13):1872-4.

39. Placone AL, McGuiggan PM, Bergles DE, Guerrero-Cazares H, Quinones-Hinojosa A, Searson PC. Human astrocytes develop physiological morphology and remain quiescent in a novel 3D matrix. Biomaterials. 2015;42:134-43.

40. Adamson RH, Lenz JF, Curry FE. Quantitative laser scanning confocal microscopy on single capillaries: permeability measurement. Microcirculation. 1994;1(4):251-65.

41. Harris GM, Raitman I, Schwarzbauer JE. Cell-derived decellularized extracellular matrices. Methods Cell Biol. 2018;143:97-114.

42. Bowers HC, Fiori ML, Khadela JB, Janmey PA, Galie PA. Cell-matrix tension contributes to hypoxia in astrocyte-seeded viscoelastic hydrogels composed of collagen and hyaluronan. Exp Cell Res. 2019;376(1):49-57.

43. Rossitti S, Stephensen H. Temporal heterogeneity of the blood flow velocity at the middle cerebral artery in the normal human characterized by fractal analysis. Acta Physiol Scand. 1994;151(2):191-8.

44. Westin JE, Lindgren HS, Gardi J, Nyengaard JR, Brundin P, Mohapel P, et al. Endothelial proliferation and increased blood-brain barrier permeability in the basal ganglia in a rat model of 3,4-dihydroxyphenyl-L-alanine-induced dyskinesia. J Neurosci. 2006;26(37):9448-61.

45. Tanweer O, Wilson TA, Metaxa E, Riina HA, Meng H. A comparative review of the hemodynamics and pathogenesis of cerebral and abdominal aortic aneurysms: lessons to learn from each other. J Cerebrovasc Endovasc Neurosurg. 2014;16(4):335-49.

46. Garcia-Polite F, Martorell J, Del Rey-Puech P, Melgar-Lesmes P, O'Brien CC, Roquer J, et al. Pulsatility and high shear stress deteriorate barrier phenotype in brain microvascular endothelium. J Cereb Blood Flow Metab. 2017;37(7):2614-25.

47. Vanhoutte PM. Endothelium and control of vascular function. State of the Art lecture. Hypertension. 1989;13(6 Pt 2):658-67.

48. Minick CR, Stemerman MG, Insull W, Jr. Effect of regenerated endothelium on lipid accumulation in the arterial wall. Proc Natl Acad Sci U S A. 1977;74(4):1724-8.

49. Alimperti S, Mirabella T, Bajaj V, Polacheck W, Pirone DM, Duffield J, et al. Three-dimensional biomimetic vascular model reveals a RhoA, Rac1, and N-cadherin balance in mural cell-endothelial cell-regulated barrier function. Proc Natl Acad Sci U S A. 2017;114(33):8758-63.

50. Zhang XJ, Li CH, Hao WL, Zhang DH, Ren CF, Gao BL. Enlarged Anterior Cerebral Artery Bifurcation Angles May Induce Abnormally Enhanced Hemodynamic Stresses to Initiate Aneurysms. World Neurosurg. 2018;120:e783-e91.

51. De Bock M, Van Haver V, Vandenbroucke RE, Decrock E, Wang N, Leybaert L. Into rather unexplored terrain-transcellular transport across the blood-brain barrier. Glia. 2016;64(7):1097-123.

52. Knowland D, Arac A, Sekiguchi KJ, Hsu M, Lutz SE, Perrino J, et al. Stepwise recruitment of transcellular and paracellular pathways underlies blood-brain barrier breakdown in stroke. Neuron. 2014;82(3):603-17.

53. Chien S. Effects of disturbed flow on endothelial cells. Ann Biomed Eng. 2008;36(4):554-62.

54. Ulm AJ, Fautheree GL, Tanriover N, Russo A, Albanese E, Rhoton AL, Jr., et al. Microsurgical and angiographic anatomy of middle cerebral artery aneurysms: prevalence and significance of early branch aneurysms. Neurosurgery. 2008;62(5 Suppl 2):ONS344-52; discussion ONS52-3.

55. Fujimura M, Gasche Y, Morita-Fujimura Y, Massengale J, Kawase M, Chan PH. Early appearance of activated matrix metalloproteinase-9 and blood-brain barrier disruption in mice after focal cerebral ischemia and reperfusion. Brain Res. 1999;842(1):92-100.